Biomaterials Science

ROYAL SOCIETY OF CHEMISTRY

PAPER

View Article Online
View Journal | View Issue

Cite this: *Biomater. Sci.*, 2026, **14**, 885

On-demand synthesis of calcium phosphate crystals in droplet micro-reactors of continuous operation

Konstantinos Tsachouridis, Ahlam Al Hadhrami and Antonios D. Anastasiou *

In this work, the use of droplet microreactors is demonstrated for the on-demand synthesis of three calcium phosphate minerals. In a simple three-inlet, flow focusing design, microdroplets serve as isolated reactors where crystals are formed under controlled conditions. Selective production of brushite, hydroxyapatite, or fluorapatite was achieved by modulating only the composition and the pH of a buffer stream without disturbing the flow regime and the continuous operation of the system. Temperature and residence time have been proved as key variables to control the properties of the resulted particles. Moving from 25 to 37 °C resulted in a more crystalline material, while by increasing the residence time from 2 to 10 min, bigger particles were obtained. Compared to the standard batch synthesis, in microfluidics, crystallisation crystals were less aggregated and smaller in size. During μ-LIF measurements, it was confirmed that the formation of the crystals affects the mixing quality within the droplets and this can be a field of improvement in order to get particles with more consistent properties. Overall, this work shows the potential of droplet microreactors as a versatile "factory-on-chip" tool for continuous production of biomaterials. Beyond calcium phosphates, the same approach provides a scalable route to precision synthesis of multiphase and composite materials, enabling new frontiers in biomedical translation and advanced manufacturing.

Received 24th September 2025,
Accepted 28th November 2025

DOI: 10.1039/d5bm01425e

rsc.li/biomaterials-science

1. Introduction

The synthesis of calcium phosphates (CaPs) has been a subject of intensive research, which is driven by the wide range of applications of these minerals in tissue engineering.[1] Their biocompatibility, regenerative potential and their chemical and structural similarity with the minerals of human hard tissues[2] make them ideal candidates for the fabrication of implants, scaffolds, bone cements and other medical devices.[3] Various synthesis methods for CaPs have been investigated on a lab scale over the years, for example sol–gel synthesis[4] and hydrothermal methods;[5] however, wet precipitation is the most well studied route due to its simplicity, low temperature and pressure, and easy translation to industrial production. One of its great advantages is that the mineral phase and the properties of the synthesised calcium phosphate crystals can be controlled by adjusting the conditions of the reaction such as temperature, pH, residence time and Ca to P ratio.[6] For example, at acidic pH (4–6), the formation of monocalcium and dicalcium phosphates (*e.g.* brushite) is favoured, while at a higher pH (>7), tricalcium phosphate and/or hydroxyapatite can be obtained.[7] On the other hand, temperature can be the means to control the crystallinity of the minerals and the characteristics of the final particles.[2] In the case of large scale production, precipitation takes place in batch, stirred tank reactors. Although the implementation of the synthesis procedure is simple and the operating cost of these reactors is low, there are issues like low mixing efficiency and heterogeneous concentration and temperature gradients that can affect the quality of the final product.[8] From the process engineering point of view, batch synthesis is more difficult to control, while the start–stop nature of batch operation increases downtime and lowers the overall productivity of the unit.

A potential solution to improve the properties of the synthesised CaPs and the efficiency of the production is the use of milli-/microfluidic reactors of continuous operation. The small volumes of fluids involved in microfluidics offer good regulation of operating conditions like reactant concentrations, temperature gradients and mass transfer rates.[9,10] As documented in the literature for various nanoparticle systems, the synthesis in microfluidics results in crystals with narrow size distributions and well-defined properties.[11,12] Amongst the advantages of microfluidics is also the potential of straightforward scaling up by operating continuously multiple parallel microreactors.[13–15] Various reactor designs have been proposed over the years for the synthesis of nanoparticles including CaPs.[6,11] A modular oscillatory flow reactor was extensively

Lab of Complex Fluids and Microfluidics, Department of Chemical Engineering, University of Manchester, Manchester, M1 3AL, UK.
E-mail: Antonios.anastasiou@manchester.ac.uk

investigated by Veiga *et al.*[16] and operating parameters like oscillation amplitude, residence time and temperature were investigated to identify how the properties of the obtained CaPs could be controlled. This type of reactor was indicated as a potential platform to satisfy the needs of industrial production. Droplet microreactors are also a viable option for the synthesis of crystals with key advantages such as the well-controlled volume of reaction (volume of the droplet) and the reduced fouling.[17] In the work of Galván-Chacón *et al.*,[18] such a device was utilised to produce a variety of CaP-based biomaterials (*e.g.* hydroxyapatite) and the formation of spherical micro-particles of controlled size and porosity was demonstrated. Tsachouridis *et al.*[19] assessed three types of droplet microreactors for the continuous production of metal oxide and CaP nanoparticles. A three-inlet, flow focusing design was identified as the most appropriate for long-term operation. The key feature of this design is a buffer, aqueous stream that keeps the raw materials separated at the droplet formation point, preventing the fouling of the crystals and the blocking of the channels. This buffer stream can be also used to tune the reaction conditions within the droplets. Motivated by this, the present work aims to explore how the phase and the characteristics of the CaP crystals could be controlled during the continuous operation of the microreactor. The main objective was to demonstrate the on-demand synthesis of three well-known CaP phases by only changing the composition of the buffer stream without disturbing the flow pattern and the general operation of the microreactor. Amongst CaPs, hydroxyapatite [HAP: $Ca_{10}(PO_4)_6(OH)_2$], brushite (DCPD: $CaHPO_4{\cdot}2H_2O$) and fluorapatite (FAP: $Ca_5(PO_4)_3F$) are three of the most well documented with a wide range of applications in orthopaedics and dentistry[7] and for this reason became the focus of this study. Brushite crystals are formed at pH < 5.5 and typically have a flake-like shape and size, reaching up to 40 microns.[20] HaP crystals on the other hand are typically formed in an alkaline environment, and they have a needle-like shape.[6] Fluorapatite is formed under the same conditions as HaP and in the presence of F^- ions it substitutes OH^- in the crystal lattice.[21] In the first stage of our study, droplet formation experiments were conducted to identify the appropriate operating conditions of the microreactor. To confirm the phase of the obtained minerals, characterisation techniques like X-ray diffraction and transmission electron microscopy were utilised. A comparison between the materials from the microfluidic synthesis and the standard batch process was made to understand the effect of the different synthesis variables.

2. Materials and methods

2.1 Fabrication of the microreactors and the experimental setup

Commercial CAD software (Autodesk Fusion 360) was used to design the microfluidic channels (Fig. 1a), which were then fabricated in a high-resolution, resin 3D printer (Sonic Mini 8 K) using a transparent, low-viscosity resin (BV007A, Creative CADworks) with absorbance at 390 nm. A thickness of 30 μm was selected for each printing layer, and the exposure time was set to 1.8 s. After printing, the microchannels were cleaned with isopropanol (IPA) and then rinsed with water to remove any residual resin. The devices were then cured for 2 min under UV light to complete the polymerization of the resin. The open microchannels (Fig. 1b) were sealed with Kapton tape (Tesa 51408) and fixed on a chip holder, between two metallic plates.

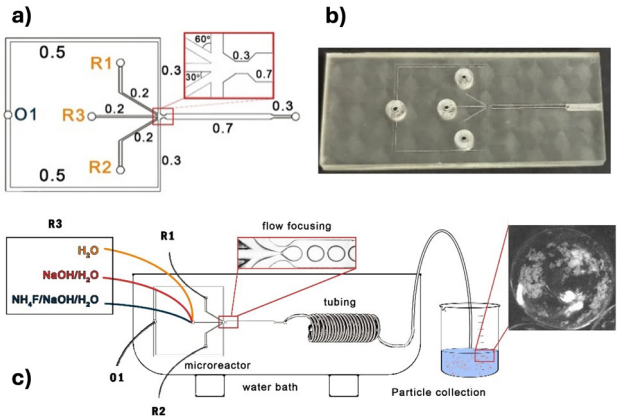

Fig. 1 Design of the microreactor and experimental setup. (a) Microfluidic channel geometry; (b) protype microreactor; (c) experimental setup for microfluidic synthesis.

For the microfluidic synthesis, based on our previous work,[19] a concentration of 0.04 M was selected for the precursor (R1; $Ca(NO_3)_2{\cdot}4H_2O$, Sigma-Aldrich, CAS:13477-34-4) and precipitation agent (R2; $Na_2HPO_4{\cdot}2H_2O$ (Sigma-Aldrich, CAS: 7558-79-4)). A high-viscosity silicone oil (100 cSt at 25 °C, Sigma-Aldrich, CAS: 63148-62-9) (O1) was the continuous phase during all the experiments. High accuracy syringe pumps (NE-1000 syringe pump) were used for the circulation of liquids and control of the flow rates. To regulate the residence time, tubing of appropriate length and inner diameter 1 mm was connected at the exit of the microreactor. The microreactor and the tubing were placed in a water bath (Cole-Parmer WB-400) to control the temperature. The droplets were collected in a beaker (Fig. 2), and the separation of the three-phase mixture (oil–water particles) was achieved in a centrifuge (FastGene® High-Speed Mini Centrifuge, Cat. No.: NG003) at 11 000 rpm. The particles were collected, washed, and then placed in a freezer at −25 °C overnight. Drying was performed in a freeze dryer (VirTis Benchtop pro) operating at 150 mTorr and −90 °C.

The synthesized materials are listed in Table 1. For brushite synthesis (R3 is H_2O solution) at 25 °C, residence times (RTs) in the microreactor (including the outlet piping) of 2 min (MBr1) and 10 min (MBr2) were used and at 37 °C RTs of 2 min (MBr3) and 10 min (MBr4) were used. The same protocol was used for the microfluidic HaP (MHaP) synthesis (R3 is

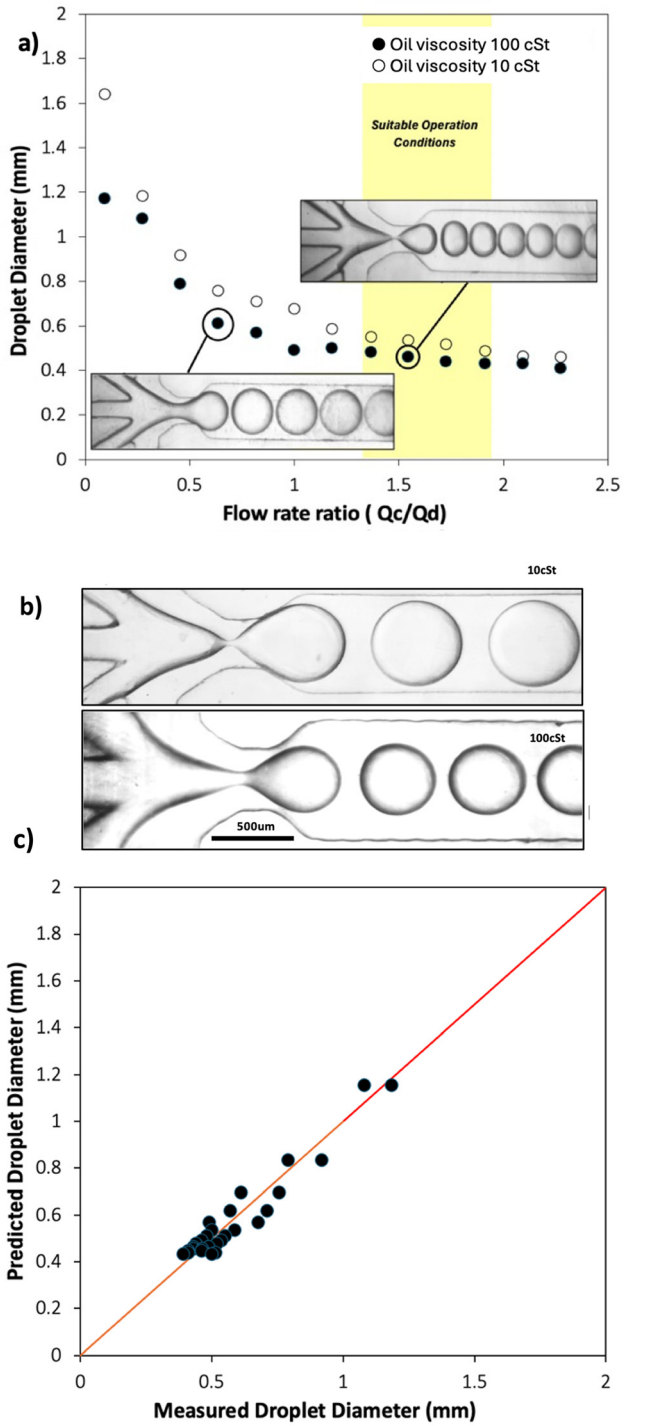

Fig. 2 Droplet formation experiments in the microreactor. (a) Droplet diameter as a function of the flow rate ratio (Q_c/Q_d) and identification of appropriate operating conditions; (b) indicative droplet size at Q_c/Q_d = 1.0 for oils 10 and 100 cSt, and (c) comparison of experimentally measured droplet sizes with predictions from the literature-based scaling law.

$NaOH/H_2O$ solution), whereas for the microfluidic fluorapatite (MFaP1), R3 was NH_4F (Sigma-Aldrich, 12125-01-8), ($NaOH/H_2O$), and only a RT of 2 min at 37 °C was explored.

Table 1 The synthesised materials and reaction conditions

Mineral	Method	Code	T (°C)	RT (min)
Brushite	Batch	BBr	37	120
	Microfluidic (R3 : H_2O)	MBr1	25	2
		MBr2	25	10
		MBr3	37	2
		MBr4	37	10
HAP	Batch	BHaP	37	120
	Microfluidic (R3 : $NaOH/H_2O$)	MHaP1	25	2
		MHaP2	25	10
		MHaP3	37	2
		MHaP4	37	10
FAP	Batch	BFaP	37	120
	Microfluidic (R3 : $NH_4F/NaOH/H_2O$)	MFaP1	37	2

2.2 Batch synthesis of CaPs

For the batch synthesis of batch brushite (BBr), a 0.1 M Ca $(NO_3)_2{\cdot}4H_2O$ aqueous solution (200 mL) was heated to 37 °C, and then a 0.1 M $(NH_4)_3PO_4$ solution (200 mL) was added dropwise. The final mixture was left under continuous stirring at 37 °C for 2 h, and then left to settle for 2 h to allow precipitation. During these steps, the top of the beaker was sealed with aluminum foil to exclude CO_2 ingress into the phosphate mineral solution. The formed brushite crystals were washed several times with distilled water and placed in a freezer at −20 °C overnight and freeze-dried. For the synthesis of batch hydroxyapatite (BHaP), the same procedure was followed, but NaOH solution was also added dropwise simultaneously with the addition of the $(NH_4)_3PO_4$ solution to maintain a pH above 10, while for the synthesis of batch fluorapatite (BFaP), a $NH_4F/NaOH$ solution was used instead.

2.3 Materials' characterisation

TEM images of calcium phosphates were obtained using an FEI Tecnai G 20 microscope at an accelerating voltage of 200 kV. TEM samples were prepared by obtaining a suspension from the particle powder in ethanol, followed by dropping it on a carbon-coated grid and drying for 2 h.

XRD measurements were conducted on a PANalytical X'Pert Pro that has a $\theta:\theta$ geometry. The X-ray source is a copper sealed tube target producing Cu kα and kβ emission lines from a generator operating at 40 kV and 40 mA. An incident beam Soller slit of 0.04 rad, 2° fixed anti-scatter slit, an incident beam mask of 10 mm, a programable automated divergence slit giving a constant illuminated length of 10.0 mm, and a Soller slit of 0.04 rad were used. Data were collected from 5 to 85° using a step size of 0.02 deg. and the time per step of 1.2 s. The datasets were analyzed using X'Pert Highscore Plus,[22] using reference patterns for brushite (PDF 09-0077), hydroxyapatite (PDF 09-0432) and fluorapatite (PDF 15-0876).

The morphology of the calcium phosphate samples was examined using an FEI Quanta 650 microscope under high

vacuum and an accelerating voltage of 10 kV. The samples were fixed on aluminum stubs and coated with a 6 nm Au/Pd (80 : 20) layer using a Quorum coater.

2.4 Droplet characterisation and mixing experiments

For identifying the appropriate operating conditions of the microreactor, droplet characterisation experiments were conducted. All experiments were monitored using a high-speed camera (AOS S-MIZE) and an inverted microscope (KERN OCM-161). Videos with a frame rate of 1500 fps were captured and frame-by-frame analysis was performed to determine the droplet size and formation rate.

Mixing within the droplets was investigated for a non-reactive system with all inlets containing deionised water and a reactive system where brushite precipitated from calcium nitrate and ammonium phosphate solutions. Measurements were obtained at four positions—droplet formation, immediately after inlet merging (6 mm), mid-channel (15 mm), and near the outlet (30 mm). Rhodamine B dye was added to one aqueous inlet to perform Micro-Laser Induced Fluorescence (μ-LIF) analysis with a system comprising a Nikon Eclipse Te200 inverted microscope, a PCO Panda 26 DS camera and a pulsed laser (LD-PS/5, Optolution). Image acquisition and processing was achieved with the use of PIVlab on MATLAB2021a.

3. Results and discussion

3.1 Droplet formation and flow conditions for CaP synthesis

Droplet formation experiments have been conducted for understanding how droplet size is affected by parameters such as the viscosity of the continuous phase and flow rate ratio and for identifying the appropriate flow conditions for the synthesis experiments. As shown in Fig. 2a, the microreactor features a triangular merging region where the three dispersed phase streams converge and droplets are formed. After the first merging of the aqueous streams, the droplet formation was stabilised to the dripping regime for a wide range of flow rates (no jetting was observed for the studied flow rates). When the two oils with a viscosity of 100 cSt and 10 cSt were tested, it was found that for the same flow conditions the high viscosity oil consistently resulted in slightly smaller droplets. This was reasonable considering that as the viscosity increases the viscous forces become higher and overcome interfacial tension (increase of capillary number).[23] The other key difference between the two oils was that for 10 cSt, pronounced merging of droplets was observed after their formation and during their flow in the microchannel and particularly at the outlet of the microreactor.

The flow rate ratio (Q_c/Q_d) was the variable with the strongest effect on droplet size. For the 100 cSt oil, increasing Q_c/Q_d from 0.1 to 0.5 resulted in a dramatic reduction of the average diameter from 1.2 mm to 0.6 mm. The minimum droplet size was achieved for $Q_c/Q_d = 2$, and further increase had practically no effect on the diameter. The experimental results were compared with a correlation proposed in the literature for predicting the droplet size;[24] scaling law was expressed as

$$D = w + w \cdot \alpha \frac{Q_d}{Q_c} \quad (1)$$

where D is the droplet diameter, w is the channel width and Q_d/Q_c is the dispersed-to-continuous phase flow rate ratio and α is an order one constant that depends on the geometry of the microreactor.[24] This model relates droplet size to the interplay between geometric confinement and flow rate of continuous and dispersed phases. As shown in Fig. 2b, the model exhibits strong agreement with experimental data, particularly for $Q_c/Q_d > 0.5$, where flow was dominated by dripping mechanisms. In this regime, the balance of interfacial and viscous forces was well captured by the scaling law. At larger droplet sizes, the model tends to overpredict, with the greatest deviation observed at 1.17 mm measured *versus* 2.99 mm predicted. Despite this, the model achieved a high correlation (R^2 = 0.787) and an average absolute error of ~13%, confirming its suitability for rapid droplet size estimation under controlled flow conditions.

Based on the results from the flow experiments, Q_c/Q_d = 1.73 and the oil viscosity of 100 cSt were identified as the appropriate operating conditions and were kept the same for all the synthesis experiments, having in mind not only the size of the droplets but also the total flow rate of the oil. To maintain an isolated reaction environment, the use of high-viscosity oil was preferred, since it stabilizes droplet boundaries, reducing the chances of merging.

3.2 CaP synthesis in microreactors

During the first synthesis, it was important to monitor the flow of the droplets and to verify that there was no merging throughout the flow path (Fig. 3). As depicted in Fig. 3a and b, the droplets maintain the same shape and size from the formation point to the entrance of the final tubing. As shown in Fig. 4b, droplets progressively lose transparency, indicating the onset of nucleation. The emergence of a solid-phase material within the droplets confirms that crystal formation begins during the transit through the channel and continues into the collection reservoir. After collection, the droplets were exam-

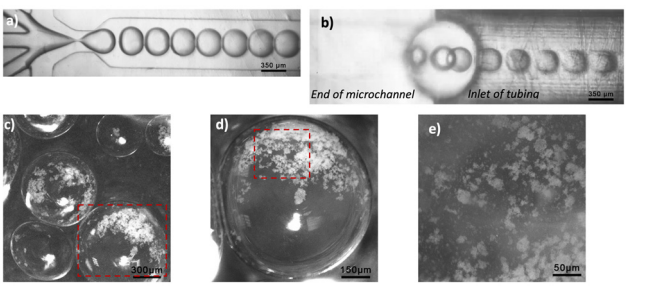

Fig. 3 Observation of the droplets during brushite synthesis. (a) Droplets at the merging chamber; (b) droplets exiting the MR and entering the microtubing; (c–e) droplets in the collection beaker and crystals inside the droplets after 10 min of synthesis.

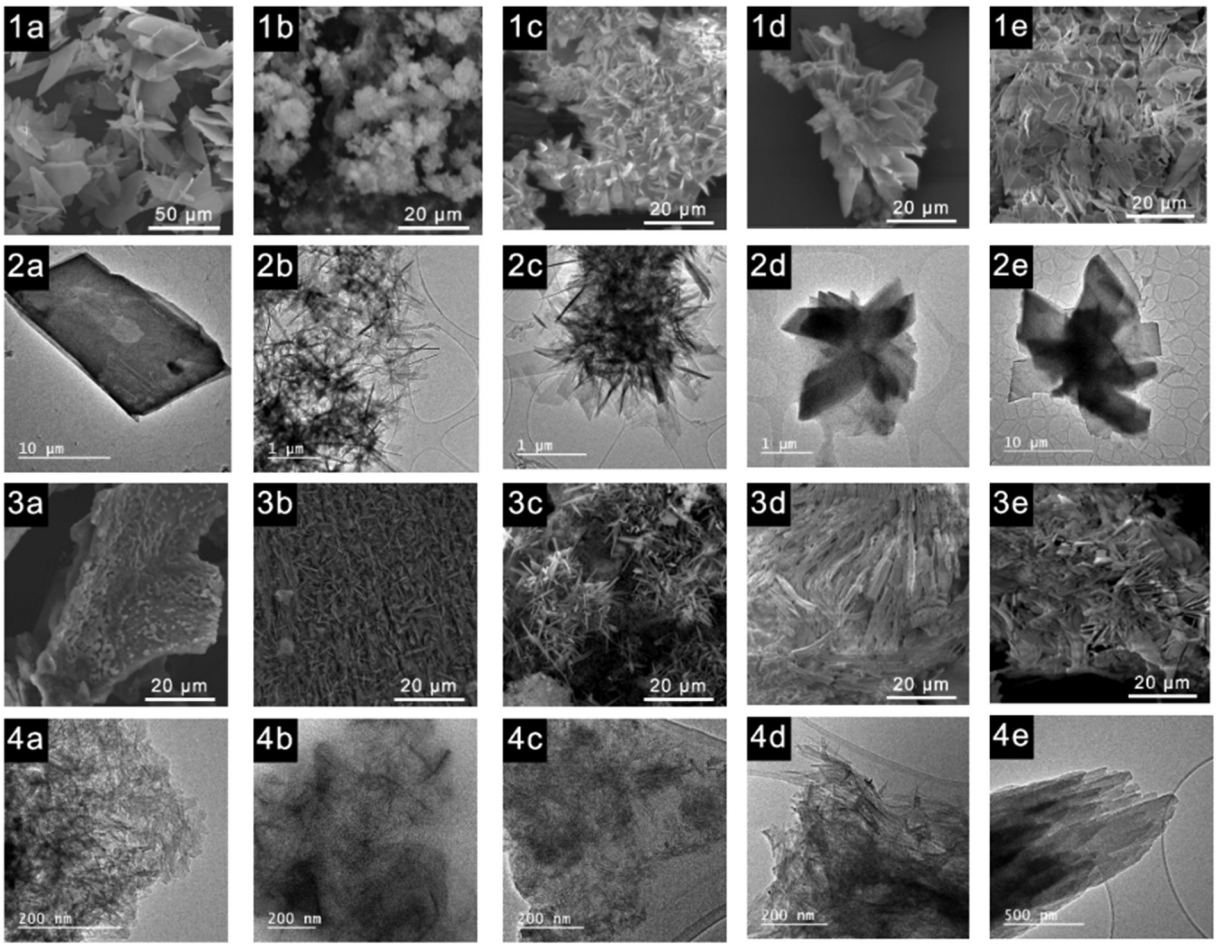

Fig. 4 Scanning and transmission electron microscopy for all the synthesised materials. First row SEM images of brushite: (1a) BBr; (1b) MBr1; (1c) MBr2; (1d) MBr3; (1e) MBr4. Second row, TEM images of brushite: (2a) BBr; (2b) MBr1; (2c) MBr2; (2d) MBr3; (2e) MBr4. Third row, SEM images of hydroxyapatite: (3a) BHaP; (3b) MHaP1; (3c) MHaP2; (3d) MHaP3; (3e) MHaP4. Fourth row, TEM images of hydroxyapatite: (4a) BHaP; (4b) MHaP1; (4c) MHaP2; (4d) MHaP3; (4e) MHaP4.

ined under a microscope; Fig. 4c–e display droplets after 10 min of synthesis time. Fine particulate material was visible inside the aqueous phase, confirming the successful in-droplet precipitation of CaPs. For all the synthesis experiments, it was confirmed that the droplet size was unaffected from the occurring reaction and matched the findings from the initial hydrodynamic experiments.

Brushite synthesis. Brushite was synthesised in the microreactor for temperatures 25 °C and 37 °C and residence times of 2 and 10 min. In the SEM and TEM images (Fig. 4), distinct morphological differences were observed between the batch and microfluidic synthesis. The materials obtained from the first (Fig. 4.1a and 2a) exhibited large-area flake-like crystals averaging slightly over 10 μm in length, indicating a less controlled growth environment. In contrast, the microfluidic samples exhibited a progression in crystal development as both the temperature and the residence time were increased. At 25 °C for 2 min (Fig. 4.1b and 2b), the flakes were underdeveloped, averaging 1.5 μm in length, indicating limited growth and potentially rapid nucleation under short exposure to the reagents. Extending the reaction time to 10 min at 25 °C (Fig. 4.1c and 2c) led to a slight increase in crystal size, with average dimensions of 2 μm in length. At a higher temperature of 37 °C for 2 min (Fig. 4.1d and 2d), the crystals were more developed, with an average length of 4 μm, highlighting the influence of increased temperature on accelerating crystal maturation. The most well-developed flakes were observed at 37 °C for 10 min residence time (Fig. 4.1e and 2e), where the crystals reached an average of 7 μm in length and up to 3 μm in width. These results suggested that both high temperature and long exposure times contribute to the formation of mature and well-structured crystals. The correlation between synthesis conditions and crystal morphology suggests that microfluidic synthesis provides greater control over the size and development of brushite crystals than batch synthesis. Also, it was clear that the formation of the crystals took place much faster in the microreactor since the materials for 10 min residence time were comparable to the batch synthesis where the reactants remained in contact longer and the precipitation lasted for several hours.

As shown in Fig. 4a, the XRD analysis verified the similarities of the materials obtained from the batch and microfluidic synthesis, indicating in all cases brushite as the dominant phase. The pattern for BBr shows a highly crystalline material (sharp, clear peaks) with all the characteristic peaks of brushite (PDF 09-0077). The microfluidic synthesis at 25 °C (MBR1 and MBR2) resulted in a less crystalline material and the characteristic peak of brushite at 11.5° had a low relative intensity, indicating underdeveloped crystals. The effect of residence time for this temperature seemed to be negligible since the two patterns for 2 and 10 min were similar. When the temperature was increased to 37 °C, the resulted crystals gave patterns closer to the ones of the batch synthesis. The materials seemed to be more crystalline compared to MBR1 and MBR2 and the peak at 11.5° was of considerable height. It is worth mentioning that the relative intensity of this peak is not only a matter of the crystal structure of the material but is also affected by the geometry of the crystals. Brushite's flake-like crystals tend to align during sample preparation, producing a strong texture effect that enhances reflections parallel to the (0 1 0) plane, with the most characteristic example the 11.6° peak.[25] This alignment arises from the intrinsic anisotropy of brushite, where the (0 1 0) plane forms the main basal face and growth along (0 1 0) is comparatively slow. The lower intensity of this reflection in the 25 °C samples (MBr1–MBr2) indicates less developed flake orientation, while at 37 °C (MBr3–MBr4) the stronger (0 1 0) peak confirms more complete development of these faces, consistent with the larger and well-defined crystals seen in SEM. Overall, it was evident that during the microfluidic synthesis, temperature is the variable that affects the crystal structure of the material most. On the other hand, the effect of residence time for brushite was more apparent on the size of the crystals and not the crystallinity or the resulted mineral phases.

Synthesis of hydroxyapatite. To switch from brushite to hydroxyapatite, NaOH was introduced in the buffer stream, aiming for alkaline conditions (pH > 8.5) within the droplets. The SEM and TEM images of the HAP crystals revealed differences in morphology between the synthesis methods. The batch obtained material (Fig. 4.3a and 4a) appeared as highly aggregated rod-like structures, with individual crystals measuring less than 200 nm in length. This aggregation may be due to the rapid nucleation and limited growth control of the batch synthesis process, resulting in densely packed nanostructures. On the other hand, the microfluidic samples displayed better defined crystal formations, with a clear trend toward increased growth as both the temperature and residence time were increased.

At 25 °C for 2 min (Fig. 4.3b and 4b), the HAP crystals formed underdeveloped needles, but with less aggregation compared to the batch method, indicating some degree of separation. Extending the reaction time to 10 min at the same temperature (Fig. 4.3c and 4c) led to more developed and bigger in size, needle-like structures. At 37 °C for 2 min (Fig. 4.3d and 4d), the crystals shifted to more well-defined rod-like shapes, reaching a few microns in size. These rods showed slight aggregation, suggesting that although higher temperatures promoted growth, there was still some tendency for the crystals to cluster. Finally, at 37 °C for 10 min (Fig. 4.3e and 4e), the crystals exhibited rod and flake-like structures that were highly aggregated, with individual crystals still in the micron range, which again suggested that prolonged contact time in the droplet promotes crystal interaction and clustering. This increase in aggregation was directly linked to the larger crystal sizes formed under these conditions.

The difference in morphology observed between brushite and hydroxyapatite resulted from the inherent crystal structures of the two phases. Brushite grows as thin plates because its lattice favours expansion of broad, flat surfaces, whereas hydroxyapatite grows as needles and rods due to its strong axial growth along the crystallographic *c*-direction. These phase-specific growth behaviours, well established in the work of LeGeros,[26] fully explain the transition from flake-like brushite to rod-like hydroxyapatite under otherwise similar microfluidic conditions.

Overall, these observations show that the microfluidic environment provides tighter control over crystal size and morphology compared to batch synthesis, although longer reaction times and higher temperatures can lead to increased aggregation, particularly in the case of the hydroxyapatite crystals. The ability to tune these parameters is critical for optimizing the material's structural properties for specific applications.

The XRD results (Fig. 5b) confirmed that in all samples, hydroxyapatite was the dominant phase since the characteristic peaks at 26° and the multiple peaks between 32° and 33° were identified. The batch synthesised material (BHaP) showed the narrowest, most intense peaks, indicating the highest crystallinity. A prolonged residence time at mild temperature allowed diffusion-limited growth and defect annealing. Microfluidic synthesis at 25 °C with a short residence time (MHaP1) yielded broader peaks, reflecting smaller crystallite sizes and higher microstrain. Extending the residence time to 10 min at 25 °C (MHaP2) resulted in slightly narrower peaks, indicating growth and partial defect annealing. Increasing the synthesis temperature to 37 °C enhanced the crystallinity even at short residence times. MHaP3 displayed sharper peaks than MHaP1, demonstrating the role of temperature in accelerating crystal growth. The combination of higher temperature and extended residence time (MHaP4) produced the most crystalline microfluidic sample, approaching the peak sharpness and intensity of BHaP.

The reflection at ~26° (0 0 2), associated with crystal growth along the *c*-axis, was more pronounced in the batch material (BHaP) and in the 25 °C samples (MHaP1–MHaP2), indicating stronger alignment along this direction at lower temperature. In contrast, the 37 °C runs (MHaP3–MHaP4) exhibited a broader and less intense (0 0 2) peak but clearer separation of the reflections between 32° and 33° [(2 1 1), (1 1 2), (3 0 0)], suggesting higher overall crystallinity and reduced texture. This behaviour implied that increasing temperature and residence time improves lattice ordering and peak resolution but weakens the preferred *c*-axis orientation, which was consistent with the morphological transition from slender needles at 25 °C to thicker, more isotropic rods at 37 °C observed in TEM.

Fluorapatite synthesis. The transition from HAP to fluorapatite (FaP) was achieved when F^- ions were introduced to the

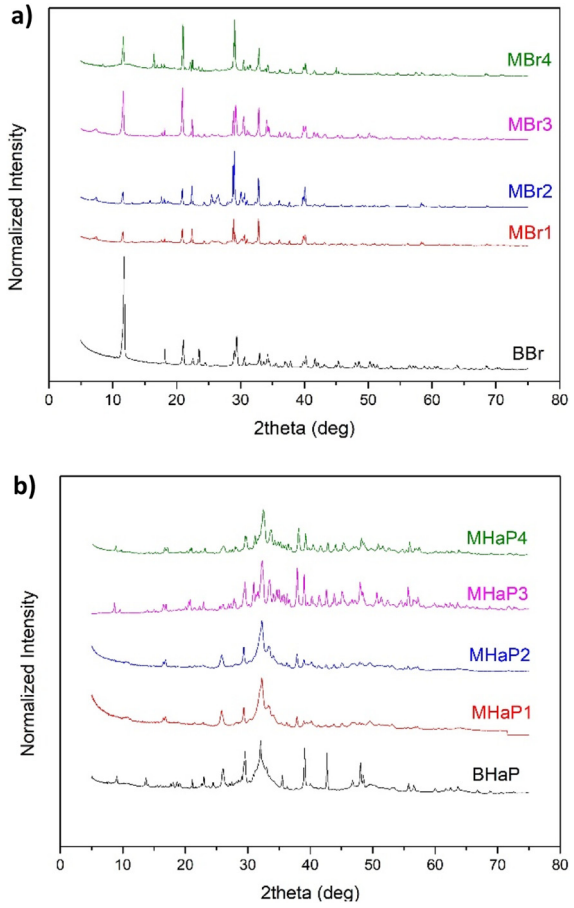

Fig. 5 Comparison of X-ray diffraction patterns for the materials obtained from the different microfluidic experiments with the batch synthesis. (a) XRD graph of brushite crystals. (b) XRD graph of hydroxyapatite crystals.

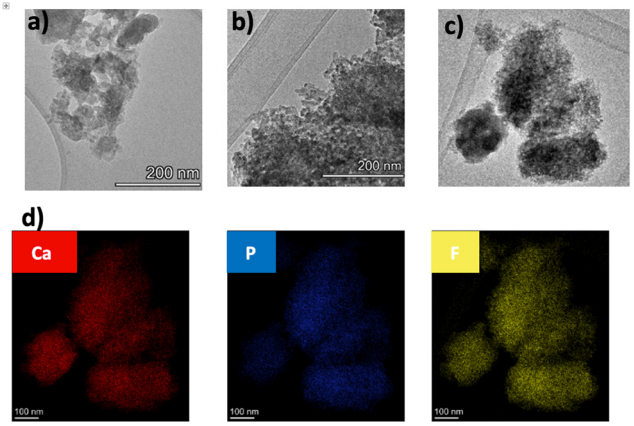

Fig. 6 Transmission electron microscopy for the fluorapatite. (a) TEM batch FaP, (b) TEM microfluidic FaP, (c) EDS spectrum and elemental analysis of MFaP, (d) TEM MFaP image used for EDS mapping, and elemental maps for Ca, P and F, respectively.

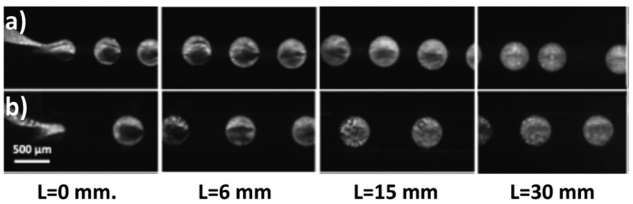

Fig. 7 µ-LIF images showing internal mixing within droplets at the merging point (L = 0 mm), post-merging (L = 6 mm), mid-channel (L = 15 mm), and channel outlet (L = 30 mm) for (a) a non-reactive system and (b) brushite synthesis at 25 °C.

buffer stream. The obtained crystals were similar to what was achieved in the batch synthesis, since in both cases small rectangular particles with smooth edges ranging from 20 nm to 100 nm were identified. Compared with the batch process (Fig. 6a), the microfluidic particles (MFaPs) imaged by TEM (Fig. 6b) were generally smaller and slightly less aggregated. Elemental analysis by STEM–EDS confirmed the successful formation of fluorapatite. The EDS spectrum (Fig. 6c) identified characteristic peaks for calcium (Ca), phosphorus (P), oxygen (O), and fluorine (F), in agreement with the expected FaP stoichiometry. Mapping of the elemental distribution across selected MFaP aggregates (Fig. 6d–g) showed a uniform spatial distribution of calcium (Ca), phosphorus (P), and fluoride (F), supporting the incorporation of fluoride within the apatite lattice.

3.3 Mixing within the droplets under reactive and non-reactive conditions

The mixing within the droplets was investigated for a reactive and a non-reactive system(Fig. 7). For the first scenario, the synthesis of brushite at 25 °C was selected. Fluorescence imaging revealed sharp dye boundaries at the merging point for both cases, confirming effective separation of aqueous streams and the absence of premixing before droplet formation. Immediately downstream, both systems exhibited a central dye-free region flanked by fluorescent zones, indicating limited initial mixing. The non-reactive system exhibited smoother radial dye diffusion, suggesting a tendency toward more homogeneous mixing, although the persistent central dark zone indicated incomplete homogenization at 15 mm distance from the droplet formation point. In contrast, the reactive system displayed pronounced internal heterogeneities characterised by irregular bright and dark patches, indicative of localised compositional variations and disrupted internal circulation likely caused by the ongoing chemical reactions and the formation of the brushite crystals. At 30 mm, droplets in the non-reactive system presented only a very narrow central dark zone surrounded by diffuse fluorescence, confirming the high degree of mixing. The droplets with reaction occurring on the other hand exhibited complex internal structures with scattered bright and dark regions, reflecting localised concentration differences and disrupted flow due to reaction-induced changes such as variations in viscosity, interfacial tension, particle formation, or phase separation. Overall, mixing was smoother and more uniform in the non-reactive system,

though neither system achieved complete homogenization within the observed timeframe. The reactive system's internal heterogeneities highlighted the significant influence of chemical reactions on droplet mixing and flow dynamics. This behavior could be explained if we considered the brushite crystals and the crystal clusters that appeared in the reactive system (Fig. 5–2b). Both can behave as moving obstacles that distort streamlines, split the two canonical toroidal vortices that are expected to appear in the microdroplets, and create stagnant pockets where diffusion dominates the mixing. The lack of fluid movement within the droplet can lead to bigger crystal clusters and regions with higher concentration gradients which influences subsequent crystal growth. Although this effect was not quantified here, it was consistent with the μ-LIF observations and explained the poorer mixing seen under reactive conditions.

Even though nucleation initiates shortly after the reagents first meet, the subsequent evolution of the crystals remains strongly dependent on the internal concentration and pH fields, which are governed by mixing. The μ-LIF results showed that reactive droplets maintain persistent compositional gradients, meaning that different regions inside the same droplet undergo different nucleation densities and experience unequal growth environments. Improving mixing reduces these gradients and produces a more uniform supersaturation field, which in turn supports a more synchronised nucleation process and more homogeneous crystal growth despite the short nucleation timescale.

4. Conclusions

This study demonstrates the use of a droplet microfluidic platform as a versatile and controllable route for the on-demand synthesis of calcium phosphate minerals. By modulating only the composition of a buffer stream, synthesis of different mineral phases, *i.e.* brushite, hydroxyapatite, and fluorapatite, can be achieved without disturbing the droplet flow pattern and the continuous operation of the system. Temperature was found to be the means to control the crystallinity of the material, while residence time had a significant effect on the size of the crystals both for brushite and hydroxyapatite. Compared to batch precipitation, microfluidic synthesis yielded smaller particles with reduced aggregation while providing enhanced control over crystal morphology and orientation, owing to the highly stable and spatially confined reaction environment that enables uniform nucleation and directional crystal growth. This acceleration was achieved without compromising the phase purity, as confirmed by XRD and elemental analysis. In microfluidics, crystals comparable to those of the batch synthesis were obtained in much shorter times. On the other hand, there was not any proof of particles with consistent properties from the microfluidic synthesis. The μ-LIF measurements revealed that chemical reactions and the formation of crystals significantly altered droplet mixing patterns, which in turn influenced the particle uniformity and crystallinity. This disruption in the flow profile within the droplet was reasonable, particularly for the case of systems like brushite where the size of the crystals was comparable to the size of the droplets. Consequently, improving mixing conditions by adding appropriate geometrical features to the microreactor design (*e.g.* stenosis and curvatures) to manipulate droplet hydrodynamics was critical for obtaining crystals of more consistent properties.

Building on the results of this study, future research should focus on integrating real-time monitoring techniques, such as in-line spectroscopy and advanced imaging, to further refine process control and improve reproducibility. Additionally, expanding the microfluidic approach to multi-phase material synthesis, including composite biomaterials, could offer new avenues for next-generation biomedical applications. Finally, collaboration with industrial partners to scale up microfluidic-based CaP production could bridge the gap between laboratory-scale research and commercial application, solidifying the role of microfluidics as a game-changing technology in biomaterial synthesis.

Conflicts of interest

There are no conflicts to declare.

Data availability

All of the raw data presented in the paper are available on Zenodo: DOI: 10.5281/zenodo.17190264.

Acknowledgements

The authors would like to acknowledge the EU-funded I-SMarD 953128 for financial support.

References

1 A. D. Anastasiou, *et al.*, Antibacterial properties and regenerative potential of Sr2+ and Ce3+ doped fluorapatites; a potential solution for peri-implantitis, *Sci. Rep.*, 2019, **9**(1), 14469.
2 S. V. Dorozhkin, Nanodimensional and Nanocrystalline Apatites and Other Calcium Orthophosphates in Biomedical Engineering, Biology and Medicine, *Materials*, 2009, **2**, 1975–2045, DOI: 10.3390/ma2041975.
3 X. Chen, *et al.*, Calcium Phosphate-Based Nanomaterials: Preparation, Multifunction, and Application for Bone Tissue Engineering, *Molecules*, 2023, **28**(12), 4790.
4 K. Ishikawa, E. Garskaite and A. Kareiva, Sol–gel synthesis of calcium phosphate-based biomaterials—A review of environmentally benign, simple, and effective synthesis routes, *J. Sol-Gel Sci. Technol.*, 2020, **94**(3), 551–572.
5 A. A. Chaudhry, *et al.*, Synthesis and characterisation of magnesium substituted calcium phosphate bioceramic nanoparticles made via continuous hydrothermal flow synthesis, *J. Mater. Chem.*, 2008, **18**(48), 5900–5908.

6 K. Lin, C. Wu and J. Chang, Advances in synthesis of calcium phosphate crystals with controlled size and shape, *Acta Biomater.*, 2014, **10**(10), 4071–4102.
7 N. Eliaz and N. Metoki, Calcium Phosphate Bioceramics: A Review of Their History, Structure, Properties, Coating Technologies and Biomedical Applications, *Materials*, 2017, **10**(4), 334.
8 A. Veiga, *et al.*, Tackling current production of HAp and HAp-driven biomaterials, *Mater. Adv.*, 2023, **4**(22), 5453–5478.
9 J. Puigmartí-Luis, Microfluidic platforms: a mainstream technology for the preparation of crystals, *Chem. Soc. Rev.*, 2014, **43**(7), 2253–2271.
10 H. Huang, *et al.*, Generation and manipulation of hydrogel microcapsules by droplet-based microfluidics for mammalian cell culture, *Lab Chip*, 2017, **17**(11), 1913–1932.
11 S. Marre and K. F. Jensen, Synthesis of micro and nanostructures in microfluidic systems, *Chem. Soc. Rev.*, 2010, **39**(3), 1183–1202.
12 S. Gimondi, *et al.*, Microfluidic Devices: A Tool for Nanoparticle Synthesis and Performance Evaluation, *ACS Nano*, 2023, **17**(15), 14205–14228.
13 T. Kamperman, *et al.*, Engineering 3D parallelized microfluidic droplet generators with equal flow profiles by computational fluid dynamics and stereolithographic printing, *Lab Chip*, 2020, **20**(3), 490–495.
14 S. Vyawahare, A. D. Griffiths and C. A. Merten, Miniaturization and Parallelization of Biological and Chemical Assays in Microfluidic Devices, *Chem. Biol.*, 2010, **17**(10), 1052–1065.
15 T. Han, *et al.*, Factory-on-chip: Modularised microfluidic reactors for continuous mass production of functional materials, *Chem. Eng. J.*, 2017, **326**, 765–773.
16 A. Veiga, *et al.*, Fabrication of calcium phosphates with controlled properties using a modular oscillatory flow reactor, *Chem. Eng. Res. Des.*, 2022, **183**, 90–103.
17 L. Shang, Y. Cheng and Y. Zhao, Emerging Droplet Microfluidics, *Chem. Rev.*, 2017, **117**(12), 7964–8040.
18 V. P. Galván-Chacón, *et al.*, Droplet microfluidics as a tool for production of bioactive calcium phosphate microparticles with controllable physicochemical properties, *Acta Biomater.*, 2021, **128**, 486–501.
19 K. Tsachouridis, Y. Zhou and A. D. Anastasiou, Comparison of three droplet microreactors for the continuous production of nano and micro particles, *Chem. Eng. Sci.*, 2024, **293**, 119956.
20 A. D. Anastasiou, *et al.*, Drug loading capacity of microporous β-pyrophosphate crystals, *Mater. Des.*, 2019, **168**, DOI: 10.1016/j.matdes.2019.107661.
21 H. Chen, *et al.*, Synthesis of Fluorapatite Nanorods and Nanowires by Direct Precipitation from Solution, *Cryst. Growth Des.*, 2006, **6**(6), 1504–1508.
22 T. Degen, *et al.*, The HighScore suite, *Powder Diffr.*, 2014, **29**(S2), S13–S18.
23 P. Garstecki, H. A. Stone and G. M. Whitesides, Mechanism for Flow-Rate Controlled Breakup in Confined Geometries: A Route to Monodisperse Emulsions, *Phys. Rev. Lett.*, 2005, **94**(16), 164501.
24 P. Garstecki, *et al.*, Formation of droplets and bubbles in a microfluidic T-junction—scaling and mechanism of breakup, *Lab Chip*, 2006, **6**(3), 437–446.
25 A. D. Anastasiou, *et al.*, Sintering of calcium phosphates with a femtosecond pulsed laser for hard tissue engineering, *Mater. Des.*, 2016, **101**, 346–354.
26 R. Z. LeGeros, Calcium phosphates in oral biology and medicine, *Monogr. Oral Sci.*, 1991, **15**, 1–201.